

Proton-proton bremsstrahlung at 280 MeV

K. Michaelian,^a P. Kitching,^a D. A. Hutchèon,^{a,b} R. Abegg,^{a,b} G. H. Coombes,^a W. K. Dawson,^b H. W. Fearing,^b H. Fielding,^a G. Gaillard,^a P. Green,^{a,b} L. G. Greeniaus,^{a,b} M. Hugi,^a C. A. Miller,^{a,b} G. C. Neilson,^a W. C. Olsen,^a J. Soukup,^a N. R. Stevenson,^c J. Wesick,^a and R. L. Workman^b

^aUniversity of Alberta, Edmonton, Alberta, Canada T6G 2J1

^bTRIUMF, 4004 Wesbrook Mall, Vancouver, British Columbia, Canada V6T 2A3

^cUniversity of Saskatchewan, Saskatoon, Saskatchewan, Canada S7N 0W0

(Received 25 April 1989)

A proton-proton bremsstrahlung experiment has been carried out at TRIUMF using a 280-MeV polarized proton beam impinging on a liquid-hydrogen target. All three outgoing particles were detected: the higher-energy proton in a magnetic spectrometer, the lower-energy proton with plastic scintillators, and the photon in lead-glass Cherenkov detectors. The experiment shows the first unambiguous evidence for off-shell effects in the free nucleon-nucleon interaction, in that the analyzing powers disagree strongly with the predictions of the soft-photon approximation (which incorporates only on-shell information) but are consistent with the results of calculations using the Bonn and Paris potentials.

I. INTRODUCTION

It is well known that even complete knowledge of the elastic-scattering amplitudes would not be enough to determine a unique potential model for the nuclear force. This is because the elastic-scattering amplitude constrains the wave functions of the particles only in the asymptotic limit where the nucleons have the momenta of free particles. What is needed to probe the off-shell contribution to the nuclear force is an interaction involving three or more bodies.

The most direct approach to obtaining off-shell information, both experimentally and theoretically, has been through reactions of the form $N + N \rightarrow N + N + \gamma$, or nucleon-nucleon bremsstrahlung. For the two-nucleon system, bremsstrahlung is the first off-shell process that occurs with increasing energy and although this is a three-body system, only two bodies are strongly interacting. This means that complications arising from other off-shell processes, for example, pion production, can be avoided by staying below the thresholds of these processes. Bremsstrahlung is also easy to handle theoretically since the form of the electromagnetic interaction is well described by QED and its weakness with respect to the strong force allows it to be treated to first order only.

Both $pp\gamma$ and $np\gamma$ experiments have been performed in the past but the data suffered from poor statistical accuracy due to the small cross sections (for a complete list of references for experiments performed prior to 1971 see the review article by Halbert;¹ more recent experiments are described in Refs. 2–8). Although at intermediate energies the $np\gamma$ cross section is approximately four times larger than the $pp\gamma$ cross section, experiments with neutrons are harder to perform, mainly because of the much lower intensities of available neutron beams. Theoretically, $np\gamma$ is also more difficult to handle because one-pion-exchange currents must be included and there are twice as many partial waves to calculate: the identity of the

protons in $pp\gamma$ allows only angular momentum singlet-even and triplet-odd states.

For these reasons a modern $pp\gamma$ experiment was initiated at the TRIUMF cyclotron facility with the objective of learning about the off-shell behavior of the strong force. Specifically the goal of the experiment was two-fold. First, we wanted to determine whether an existing modern potential would fit off-shell experimental data, particularly analyzing powers, which would be measured for the first time. To this end, a recent calculation with input from the Paris and Bonn potentials was initiated at TRIUMF. Second, the reasons why previous bremsstrahlung experiments seemed to be in better agreement with a soft-photon-approximation (SPA) calculation, which contains no off-shell input, than with potential model calculations, needed investigation. The SPA is expected to be valid only in the on-shell limit, i.e., where the photon's momentum goes to zero. Such agreement could only indicate cancellation in the off-shell terms for the bremsstrahlung process. Modern calculations of $pp\gamma$ with input from the Paris and Bonn potentials, as well as the SPA, had shown that the analyzing powers were sensitive to the differences between the potential models and the SPA, particularly at small proton scattering angles.^{9,10}

A proton energy of 280 MeV was chosen in order to stay below the pion production threshold and also as a compromise between too high an energy, where potential models would not be valid, and too low an energy, where the cross section is smaller and approaches on-shell predictions. Proton polar angles between 10° and 30° were detected. For a given incident energy, the interaction is most off shell at the smallest proton polar angles. The limit of 10° was set by the interference between the detectors and the beam line.

At the energy of this experiment the on-shell momentum p_{on} , defined as the center-of-mass momentum (or half the relative momentum) of the on-shell nucleon pair,

ranged up to 1.8 fm^{-1} whereas the off-shell momentum p_{off} , similarly defined as the center-of-mass momentum of the off-shell nucleon pair, could be as much as 2.5 fm^{-1} . The difference $|p_{\text{on}} - p_{\text{off}}|$, which measures the degree by which the process is off shell, is a very complicated function of the geometry and is different for each of the four possible Feynman diagrams contributing to any one experimental point. For the smaller-angle pairs it ranged up to about 1.5 fm^{-1} and was generally smaller than this for the large-angle pairs. Thus the present experiment is sensitive to nucleon-nucleon amplitudes which are off shell by up to 1.5 fm^{-1} .

Important features of this experiment include a liquid-hydrogen target, providing a convenient experimental geometry; detection of all three final-state particles, greatly reducing background; and track-defining counters designed to be tolerant of the large elastic background fluxes that constitute the main experimental background. Sufficient beam time was available, approximately 1000 h, to give an order-of-magnitude improvement in statistics.

II. EXPERIMENTAL METHOD

A. Overview

The experimental setup is shown in Fig. 1. A 280-MeV polarized proton beam of approximately 13 nA was extracted through TRIUMF beam line 1B. Beam polarization and intensity were monitored with a polarimeter which counted left and right coincidences for pp elastic scattering in a CH_2 target. Beam current was also measured by a secondary emission monitor (SEM) located downstream of the target and calibrated against a Faraday cup shortly after the data-taking runs.

The liquid-hydrogen target was contained within an

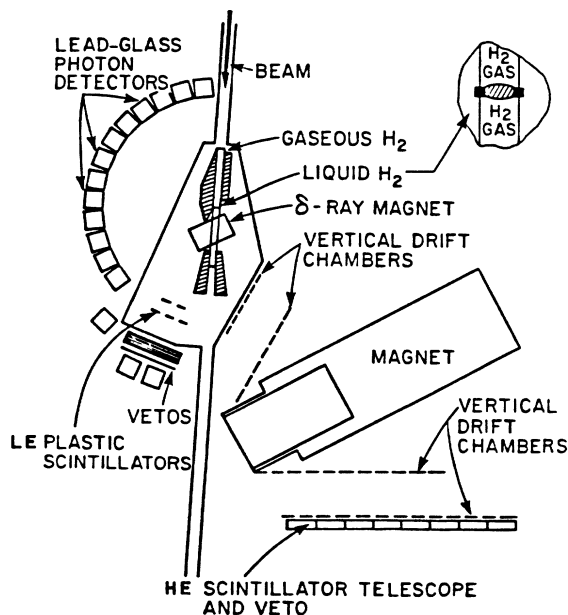


FIG. 1. Experimental setup for detecting bremsstrahlung events.

evacuated scattering chamber. The target vessel consisted of a long cylindrical flask 6.8 cm in diameter, oriented along the beam. Only a central 5-mm-thick central cell, 1.59 cm in radius, contained liquid hydrogen. Next to the liquid, on both sides, was 487.5 mm of H_2 gas at 1 atm pressure, separated from the liquid by thin $7.6\text{-}\mu\text{m}$ Kapton windows coated with 1000 Å of copper. The gas provided spatial separation of the thick beam entrance and exit windows from the liquid target region. Background originating from the entrance and exit windows was then reduced by shielding the detectors and rejecting in software the events that came from these regions. The two final-state protons were detected within a few degrees of the horizontal plane containing the beam line, and in a polar angle regime of $\sim 10^\circ$ to 30° on both sides of the beam line.

Because the detection systems of the two protons differed, in what follows a distinction will be made by referring to the proton detected on the same side of the beam line as the photon as the "low-energy proton" (LEP) and that detected on the opposite side as the "high-energy proton" (HEP).

The LEP's were detected inside the evacuated scattering chamber because in certain kinematic regions of interest the energy of the proton was as low as 4 MeV. Five 6.4-mm-thick plastic scintillators, each subtending approximately 4° at the target, were used to obtain energy and time-of-flight information and formed part of the event trigger.

The HEP was momentum analyzed with a spectrometer consisting of a "C" type dipole magnet and four vertical drift chambers (VDC's) which measured horizontal track coordinates. The initial proton scattering angle and the location of the event vertex within the target cylinder were determined using the track coordinates from the two chambers in front of the magnet. The VDC immediately in front of the magnet also measured vertical coordinates. Two chambers after the magnet, in conjunction with those in front, allowed the proton horizontal bend angle through the dipole magnetic field to be measured, i.e., a measure of its momentum. The high flux of elastically scattered protons in the VDC's was accommodated by operating at low gas gain ($\approx 10^4$) and using independent TDC-per-wire readout. The drift cell design provided at least three drift time measurements from each chamber plane for every track. These three data gave information on the track coordinate, time of passage of the particle, and a crude estimate of the angle the particle trajectory made with the wire chamber. The resolution in time and angle was sufficient to reject most extraneous coordinates recorded with $pp\gamma$ events.

An array of eight 3.2-mm-thick plastic scintillators, parallel to and directly behind the final VDC, gave the time of flight of the HEP and formed part of the event trigger. The high-energy protons were detected with this apparatus positioned in two configurations. The large-angle configuration (LAC) observed protons within polar angles of 20° to 30° , while the small-angle configuration (SAC) covered the range from 10° to 20° .

Sixteen lead-glass Cherenkov counters, spanning the polar range 15° to 170° on the same side of the beam line

as the LEP detectors, gave the approximate energy and scattering angle of the photon. Eight of them were cubes 15 cm on a side and eight were cylinders 12.7 cm in diameter by 17.5 cm deep. A cube subtended about 11° at the target, while a cylinder typically subtended 5° .

B. Background suppression

Simultaneous detection of all three final-state particles was carried out to reduce backgrounds. However, the random triple-coincidence rate observed in preliminary test runs, approximately 60 000 per second at a current of 12 nA, was still much too high to be tolerated by our acquisition system. By far the biggest contribution to this rate came from pp elastic scattering in conjunction with beam-induced neutron background triggering the Cherenkov counters.

Some of this background was reduced with a combination of energy degraders and veto counters behind both the LEP and HEP scintillators. Behind the eight trigger scintillators on the HEP side were copper plates thick enough to absorb the highest-energy $pp\gamma$ proton allowed by the kinematics plus an allowance of approximately 3% for range straggling. The plates were thin enough to allow elastic protons to penetrate and be detected by the veto counters. These veto counters were 3.2 mm thick, oversized plastic scintillators put in anticoincidence with the HEP detectors. A similar absorber-veto combination was used on the LEP side except that CH_2 was used as the absorbing material in order to minimize photon losses to the two Cherenkov detectors behind. The proton detectors were shielded by steel absorber from viewing directly the target cylinder end windows (except for the upstream window on the LEP side, for which Teflon was used to reduce photon absorption). A 3.2-mm-thick plastic scintillator in front of each Cherenkov counter vetoed charged particles.

In addition to the background flux of elastically scattered protons, a large neutron component, probably from (p, n) interactions at the beam dump, was observed during a sweep of the experimental area with a liquid scintillator. The large flux made it necessary to place two large scintillators, spanning the HEP detector region, in coincidence with the HEP trigger scintillators.

C. Detector calibration

The energy range of interest for the LEP's was approximately 10 to 120 MeV. This meant that the energy deposited by the lowest-energy proton in the 6.4-mm plastic scintillator, considering energy loss in traversing the liquid- H_2 target, was about 4 MeV. The energy deposited by the highest-energy "passing" proton was about 3 MeV. Gains of the phototubes and discriminator thresholds were set to accept all energies above 1 MeV.

The energy range of the HEP's was 50 to 220 MeV. Gains and discriminator thresholds were adjusted to accept the minimum energy (1.2 MeV) deposited in the 3.2-mm plastic scintillator.

Minimum-ionizing cosmic-ray muons were utilized for calibration of the Cherenkov detectors. It had been

determined, through calibration of the detectors in a 70-MeV electron beam, that these muons produce about the same amount of light as a 100-MeV photon in the cylindrical 12.7-cm-diameter \times 17.8-cm Pb glass, and a 120-MeV photon in the 15.2-cm cubes. Gains of the phototubes were adjusted so that the broad cosmic-ray peak (minus the pedestal) lay somewhere between $1/3$ and $1/2$ of the available ADC range. Cosmic-ray events were acquired for all 16 counters by requiring a coincidence between a Cherenkov and its veto, with discriminator thresholds turned down.

The $pp\gamma$ photons had energies ranging from approximately 190 MeV at forward angles to 50 MeV at backward angles. Thresholds were set at roughly 20 MeV by assuming that the response was linear between the pedestal and cosmic-ray peak.

Anode plane voltages of the VDC's were set to values giving the best efficiencies without drawing excessive current. The efficiencies were obtained by triggering on coincidences between any HE detector and its veto (pp elastic events). The efficiency of a chamber was taken as the fraction of events for which a hit was registered when the central region of the neighboring chamber was hit.

D. Detector timing

Relative timing of all plastic detectors and their vetos was obtained by using a gamma-gamma coincidence (from positron annihilation in a ^{22}Na source) between a movable "wand" scintillator and each particle detector in turn. Widths of the LEP, HEP, and photon detector pulses at the master gate were set to 130, 90, and 10 ns, respectively; therefore, photon detection determined the event timing. Timing errors were estimated to be ± 2 ns. The Pb glass photon detectors were timed relative to the "wand" using an Am-Be gamma source to provide coincidences when a 4.4-MeV γ -ray Compton scattered in the wand and then reinteracted in the Pb glass counter.

E. Event collection

A triple-coincidence required satisfactory pulse heights at the discriminators from at least one of each of the detector types, and the correct veto anticoincidences. For such an event times and pulse heights were encoded for the LEP and HEP scintillators and the Cherenkov counters, and the HEP track was recorded by the VDC's. The time of the event with respect to the beam microstructure period was also recorded.

To determine the amount of background from accidental coincidences, two types of events were recorded, "prompt" and "delayed." A "prompt" event was one in which all three final-state particles came from the same beam burst. These could be either real $pp\gamma$ events or random triples. A "delayed" event was one in which at least one of the particles came from a different beam burst and was therefore definitely a random event. The component of random triples mixed in with the real prompt $pp\gamma$ events was then determined from the number of delayed random events.

A small sample of pp elastic events, requiring a HEP

trigger scintillator and its elastic veto in coincidence, was acquired simultaneously with triplet coincidences for cross-section normalization. Also collected were pulser events, obtained by firing light-emitting diodes attached to each particle detector. These were used to monitor gain shifts and the dead time of the system. Dead time was obtained from the ratio of the number of pulses recorded on tape to the number submitted to the system.

In a large-angle configuration (LAC), corresponding to HEP detector between 20° and 30° , approximately 80 000 $pp\gamma$ events were obtained out of a background of some 10^7 random triple events. In a small-angle configuration (SAC), corresponding to HEP detection between 10° and 20° , approximately 60 000 $pp\gamma$ events were obtained out of an even larger background. (The cross section for the major background contributor, pp elastic scattering, increases as the HEP scattering angle decreases.) In total some 200 data tapes were obtained, each containing about 120 000 events of which only 0.6% were $pp\gamma$ events.

III. ANALYSIS

Analysis of the data consisted of applying limits on various kinematic quantities for the event as enumerated below.

(1) Since the microstructure of the incident beam consisted of 5-ns bursts of protons spaced 43 ns apart, an event was accepted only if a single Cherenkov counter fired (i.e., it was not a photon multiple) and the Cherenkov rf time as within ± 6 ns of the peak attributed to prompt events. In this way delayed, beam-induced background was removed. Multiple-photon events were rejected because timing information was obtained using a common-start-delayed-stop technique. Losses due to multiple-photon detection were estimated to be 2%. The lower part of Fig. 2 is a spectrum of Cherenkov rf time summed over all 16 counters. The peaks are broadened by adding all 16 counters together. The upper curve shows the sum over all detectors after background elimination (cuts on target position, good track reconstruction, multiple-photon rejection, HE bend angle, LE proton energy, and LE and HE proton time-of-flight) and correction for timing differences between the photon counters.

(2) The event was required to come from the liquid portion of the target. This was determined by a cut on the HEP track projected back to a plane parallel to the upstream drift chambers passing through the target center. The distribution of observed events under different target conditions is shown in Fig. 3.

(3) Those events with a single hit in each type of detector were binned according to LE detector number, Cherenkov counter number, and HE scattering angle (the full 10° to 30° coverage was divided into six 3.3° bins), giving 480 bins in all. After enough statistics had collected in each bin, spectra were plotted and limits of the following kinematic quantities determined: (a) bend angle of the HE proton in traversing the dipole magnet, (b) deposited energy in the LE proton detector, (c) time of flight

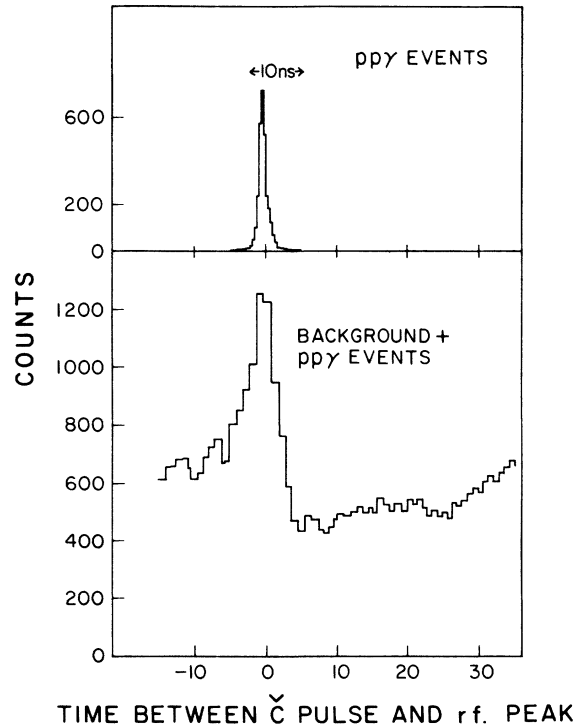


FIG. 2. Cherenkov rf time spectrum summed over all 16 Cherenkov detectors.

for the HE protons, after corrections for kinematics, delays and flight-path length differences, and (d) time of flight for the LE protons after similar corrections.

All these cuts were necessary to select good $pp\gamma$ events from the large random background. Each individual constraint was conservative so that a negligible fraction of $pp\gamma$ was lost. The data were analyzed with several values for the cuts to ensure that the results were not being biased. Figures 4 and 5 show plots of the HE bend

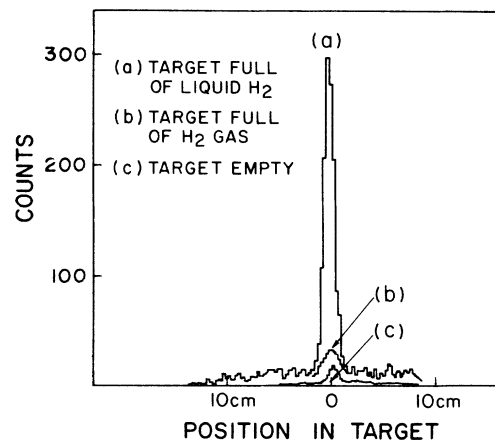


FIG. 3. Projection of the HE proton tracks in drift chambers 1 and 2 back to the target.

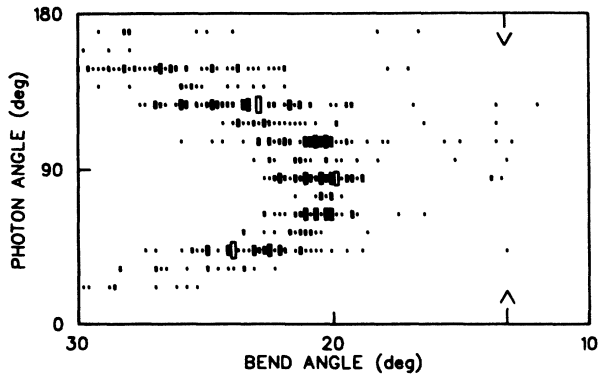


FIG. 4. HEP bend angle through the spectrometer vs photon scattering angle (HEP bin centered at 17.5°). The arrows indicate the position where pp elastic events would be located.

angle and the LE deposited energy, respectively, with all other cuts applied. In the plot of the HE proton bend angle (Fig. 4), the arrows to the right of the $pp\gamma$ events indicate the position where pp elastic events would be seen if only rf and target position constraints had been used.

Events surviving all cuts designed to eliminate background and pp elastic events were binned according to: beam polarization state (up, down, off), HEP scattering angle (by dividing the horizontal VDC coverage into four sections), LEP scattering angle (according to detector hit), and whether a prompt or delayed event.

Multiple tracks in the VDC's were resolved by first comparing the crude, internally determined track angles in neighboring VDC's and second by projecting tracks before and after the magnet to the middle of the magnet and selecting the set that was best matched. Corrections for unresolved multiples and multiple detector hits were applied to the accumulated event counts within each bin.

The empty-target background was determined by analyzing, in the same way, data taken with the target completely evacuated. This was found to be less than 0.5% of the $pp\gamma$ coincidences.

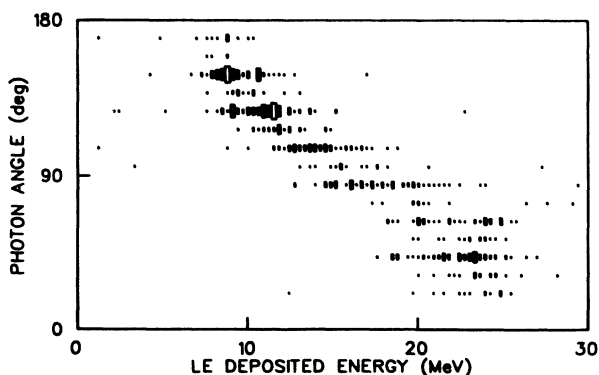


FIG. 5. LEP deposited energy vs photon scattering angle.

IV. MONTE CARLO

A. Introduction

In computing cross sections that could be compared with theoretical calculations, the efficiencies, multiple scattering, and phase-space acceptances inherent in our experimental system had to be accounted for. For this the entire experiment was simulated in a Monte Carlo software code which was developed from the three-body event-generating routine GDECA3 of the CERN GEANT library. Events were generated within the target by observing conservation of energy and momentum, kinematics, and folding in phase space and cross section, and then tracking these events through the experimental setup to their trigger counters.

A beam proton was created at the entrance to the long H_2 target cylinder. Its coordinates at entrance were chosen at random from a realistic Gaussian beam profile and its energy chosen at random from a Gaussian distribution centered at 280 MeV. The proton was then tracked with multiple scattering and energy loss through the intervening materials to a depth chosen at random within the 5 mm of liquid-hydrogen target.

The particles were tracked through the rest of the system twice. First, in the "ideal" case, the particles were not scattered after generation and the number of events that fell within the nominal solid-angle acceptances were counted. In the second trace, the "real" case, events falling within the solid angles specified by the detectors were counted and all the physics that could affect the particle on its trip to the trigger counters was taken into account. This included multiple scattering and energy degradation as the protons traversed different materials, Compton scattering and pair production of the photon, the effect of the magnetic field on the protons, and also various inefficiencies in the particle detection systems. These "real" events then represented what was actually detected by our system while the "ideal" events represent what we could have measured given the theoretical cross sections and an ideal detection system. The ratio of "ideal"/"real" events, for a given bin, represented the correction factor that had to be applied to our measured data before they could be compared with theory.

To some extent, the particular theoretical cross section folded into the event generation biases the values of these correction factors. However, biases arise only from the differences in the theoretical predictions over a particular bin since both the "real" and "ideal" events have this same cross section folded in. The difference in the cross sections derived from the Paris and Bonn potentials is small. Cross sections derived from the Paris potential were used in the event generation.

The ratio of "ideal"/"real" was calculated as described in the Appendix and used to correct the experimental counts in a given bin before the cross sections were formed. These correction factors ranged between 7 and 30 for most bins but in some cases increased to as high as 100, mainly because of the small solid angle of the Cherenkov counters. (The "real" photon detectors only observed a small portion of the azimuthal angle spanned

by the “ideal” photons.)

It was not deemed necessary to simulate the elastic events used for cross-section normalization since their detection system was relatively simple.

V. $pp\gamma$ ANALYZING POWERS AND CROSS SECTIONS

A. Analyzing powers

The analyzing powers for each bin were obtained from the accumulated counts according to

$$A_y = \frac{(N^\uparrow - R^\uparrow)/n_{\text{inc}}^\uparrow LT^\uparrow - (N^\downarrow - R^\downarrow)/n_{\text{inc}}^\downarrow LT^\downarrow}{P^\downarrow(N^\uparrow - R^\uparrow)/n_{\text{inc}}^\uparrow LT^\uparrow + P^\uparrow(N^\downarrow - R^\downarrow)/n_{\text{inc}}^\downarrow LT^\downarrow}. \quad (1)$$

Here $N^{\uparrow(\downarrow)}$ is the number of prompt events with spin up (down) passing all $pp\gamma$ tests, and $R^{\uparrow(\downarrow)}$ is the corresponding number of random events. The number of incident protons $n_{\text{inc}}^{\uparrow(\downarrow)}$ was proportional to the total charge collected by the SEM, and the system live time $LT_{\text{inc}}^{\uparrow(\downarrow)}$ was obtained from the number of pulser events submitted to the system and those recorded on tape; the live time was typically 80%.

The beam polarization was determined by observation of pp elastic scattering from a CH_2 target at 17° in the laboratory. The recoil protons were detected in coin-

idence to reduce ($p, 2p$) background. The contribution from the background was determined from separate runs with a ^{12}C target. The ($p, 2p$) contribution was found to be 9.9% and resulted in an effective analyzing power for CH_2 of 0.372. The corresponding pp elastic analyzing power¹¹ would have been 0.397. The average beam polarization, $P^{\uparrow(\downarrow)}$ in Eq. (1), was about 75%.

The analyzing powers and their statistical errors are plotted in Figs. 6 and 7 along with theoretical calculations for the Bonn and Paris potential models, as well as the soft-photon approximation (SPA).¹² For LE angles 14° and 22° , two adjacent LE bins were added together to improve the statistics. Angles listed on these plots correspond to the center of an 8° -wide LE bin. The plots at an LE angle of 28° contain only a single bin 4° wide. The HE bins for all plots are 5° wide. The abscissa is photon detection angle, divided into 16 bins whose width ranged from approximately 5° for the cylindrical counters to approximately 11° for the cubical counters.

The theoretical values, 18 Cherenkov angles equally spaced between 0° and 180° for each HE/LE angle bin, have been taken as the average of four coplanar points equally spaced within the HE and LE bins. The uncertainty in the averaging procedure to determine the theoretical cross sections, estimated by evaluating some central values using a 16-point grid, is generally less than 2% (the worst case being approximately 6% at the larg-

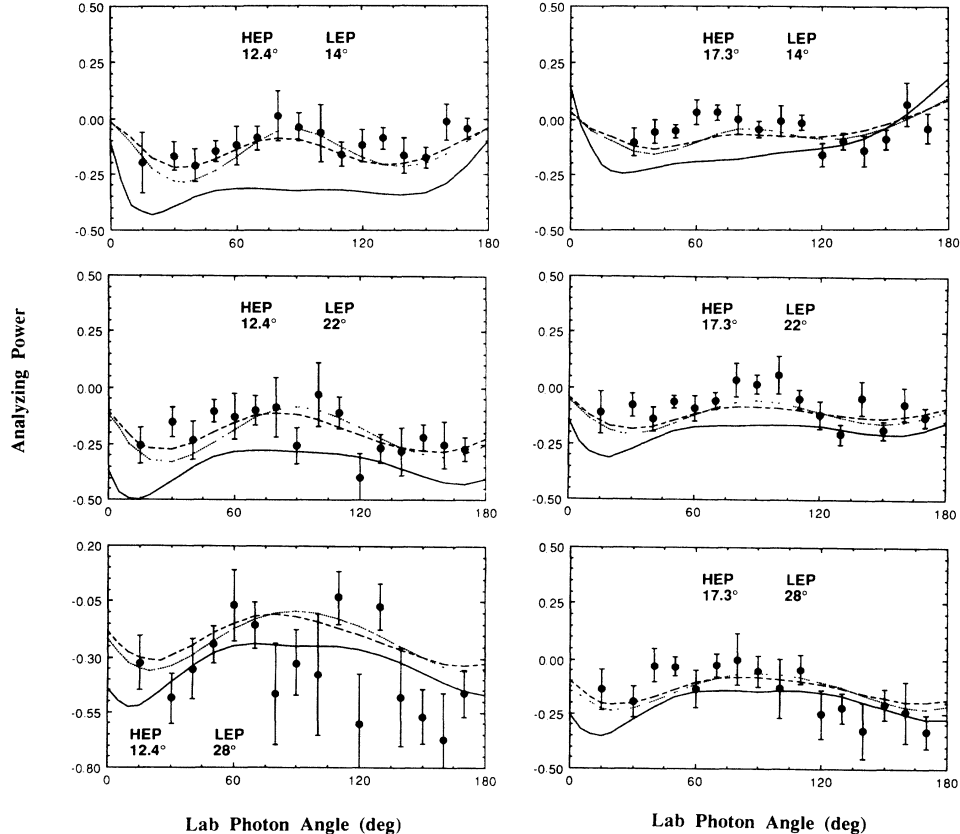


FIG. 6. $pp\gamma$ analyzing powers for the SAC mode, together with theoretical curves calculated with the soft-photon approximation (solid line), Paris potential (dotted line), and Bonn potential (dashed line).

est photon detection angle). The only systematic errors in the experimental analyzing powers are those arising from a 1.5% uncertainty in the incident proton beam polarization. This has a contribution of 1% from uncertainty in the analyzing power of hydrogen,¹¹ and from a 1% uncertainty in instrumental effects in the polarimeter.

The data points plotted in Figs. 6 and 7 are also listed in Table I.

B. $pp\gamma$ cross sections

The threefold unpolarized differential cross sections $d^3\sigma/d\Omega_{\text{HE}}d\Omega_{\text{LE}}d\theta_\gamma$, were determined from

$$\sigma_p = \frac{Z}{P^\uparrow + P^\downarrow} \left[\frac{P^\downarrow(N_R^\uparrow)}{n_{\text{inc}}^\uparrow LT^\uparrow} + \frac{P^\uparrow(N_R^\downarrow)}{n_{\text{inc}}^\downarrow LT^\downarrow} \right] \quad (2)$$

for the polarized-beam data and

$$\sigma_0 = Z \frac{N_R^0}{n_{\text{inc}}^0 LT^0} \quad (3)$$

for the unpolarized-beam data, where σ is short for $d^3\sigma/d\Omega_{\text{LE}}d\Omega_{\text{HE}}d\theta_\gamma$ and $N_R = N - R$. Here $Z = \epsilon(\Delta\Omega)/\Delta\Omega n_{\text{tgt}}$, where $\epsilon(\Delta\Omega)$ is the Monte Carlo correction factor for a given bin, $\Delta\Omega = \Delta\Omega_{\text{HE}}\Delta\Omega_{\text{LE}}\Delta\theta_\gamma$. n_{tgt} is the number of target protons in the path of the beam as determined from analysis of the prescaled HE elastic events, N_R^{el} , and the known¹¹ elastic scattering cross section σ_{el} , by the relation

$$n_{\text{tgt}} = \frac{\epsilon_{\text{el}}(\Delta\Omega_{\text{el}})}{\Delta\Omega_{\text{el}}} \frac{N_R^{\text{el}}}{n_{\text{inc}} LT} \frac{1}{\sigma_{\text{el}}}. \quad (4)$$

The solid angle for elastics $\Delta\Omega_{\text{el}}$ was determined by one of the HE scintillators in the center of the full angle range, and was only about 1.5° in size. The ratio between the value of n_{tgt} thus determined and the value calculated from the nominal target thickness of 5 mm was 0.770 (LAC) and 0.776 (SAC). This discrepancy is larger than expected, but may arise from pressure differences between the thin-walled liquid cell and the surrounding hydrogen gas. The solid angle $\Delta\Omega_{\text{LE}}$ subtended by the LE plastic scintillators was 6.09 msr. The solid angle $\Delta\Omega_{\text{HE}}$ was determined from a software analysis cut applied to the x and y coordinates of the drift chamber just upstream of the dipole C magnet. (This cut was also used in the selection of both the “real” and “ideal” Monte Carlo events.) The polar angle subtended by a particular Cherenkov counter $\Delta\theta_\gamma$ had values ranging from 4.4° (cylinders) to 10.7° (cubes). N^0 , R^0 , LT^0 , and n_{inc}^0 have the same definitions as $N^{\uparrow(\downarrow)}$, $R^{\uparrow(\downarrow)}$, $LT^{\uparrow(\downarrow)}$, and $n_{\text{inc}}^{\uparrow(\downarrow)}$ except that they are for the unpolarized beam.

The unpolarized differential cross sections, combining the unpolarized with the polarized data, are

$$\sigma = \frac{\sigma_p/(\delta\sigma_p)^2 + \sigma_0/(\delta\sigma_0)^2}{1/(\delta\sigma_p)^2 + 1/(\delta\sigma_0)^2}. \quad (5)$$

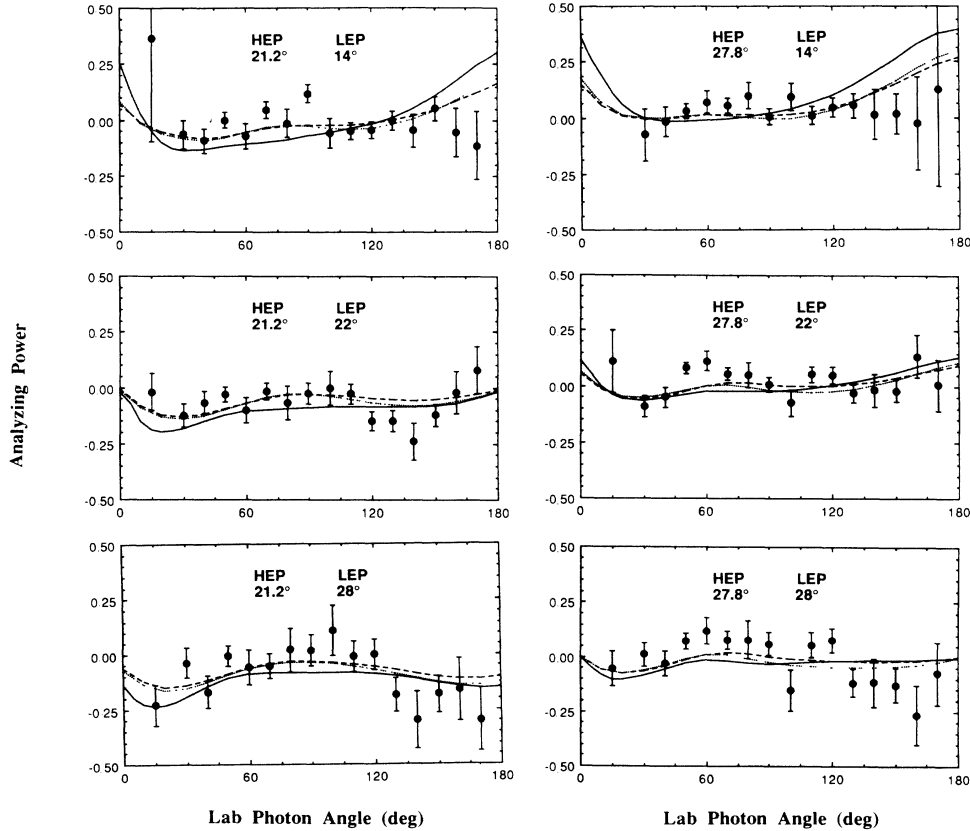


FIG. 7. $pp\gamma$ analyzing powers for the LAC mode. Theoretical curves as in Fig. 6.

Cross sections with statistical errors are plotted in Figs. 8 to 11, along with theoretical curves for the Bonn, Paris, and soft-photon approximations. The data are normalized by multiplying by a factor of 2/3 to facilitate comparison with the theory. (A discussion of this factor is left to the section on results.) The data points plotted in Figs. 8 to 11 are also listed in Table II *with this normalization constant*.

Because of the sensitivity of the Monte Carlo correction factors to the amount of absorbing material and angle of bend through the magnet for lower-energy protons, we include only those cross sections for which less than 10% of the "real" events were lost due to the following effects: (1) penetration of the higher-energy LE protons through the CH₂ absorbers and into the veto counters; (2) complete absorption of lower-energy HE protons before they reached the trigger counters; (3) lower-energy HE

protons being bent into the end 20-cm region of the HE detector array. Detection of these events will be very sensitive to the amount of energy-degrading material before the C magnet.

As with the analyzing powers, the theoretical cross-section curves have been averaged (with a cross-section weight) over four coplanar points within the HE and LE bins. The errors introduced by this averaging are in general much smaller than the statistical errors of the data, except at the largest photon scattering angles where they become comparable in size.

In considering the systematic errors in the cross section we first note that since the bremsstrahlung cross sections were normalized to the elastic cross sections, some uncertainties which were the same for both detection systems cancel and need not be considered. These include the target thickness, computer dead time, and the num-

TABLE I. $pp\gamma$ analyzing powers. Estimated scale uncertainty is 1.5%.

θ_γ (deg)	SAC small HE angles (12.4°)			SAC large HE angles (17.3°)		
	LE angle 14.0° A_y	LE angle 22.0° A_y	LE angle 28.0° A_y	LE angle 14.0° A_y	LE angle 22.0° A_y	LE angle 28.0° A_y
15.0	-0.199±0.137	-0.255±0.079	-0.326±0.120	-0.879±0.554	-0.110±0.092	-0.138±0.095
30.0	-0.170±0.063	-0.152±0.066	-0.487±0.114	-0.104±0.064	-0.076±0.051	-0.195±0.070
40.0	-0.213±0.073	-0.233±0.086	-0.353±0.136	-0.057±0.055	-0.140±0.055	-0.029±0.078
50.0	-0.148±0.046	-0.104±0.049	-0.242±0.082	-0.055±0.031	-0.063±0.030	-0.033±0.044
60.0	-0.122±0.087	-0.127±0.101	-0.068±0.161	0.030±0.058	-0.093±0.057	-0.137±0.087
70.0	-0.089±0.054	-0.101±0.064	-0.155±0.103	0.029±0.035	-0.059±0.037	-0.027±0.055
80.0	0.011±0.112	-0.087±0.131	-0.466±0.230	-0.004±0.067	0.035±0.076	-0.002±0.119
90.0	-0.038±0.063	-0.254±0.080	-0.324±0.148	-0.051±0.038	0.015±0.043	-0.056±0.071
100.0	-0.065±0.128	-0.031±0.142	-0.378±0.275	-0.012±0.071	0.057±0.085	-0.134±0.136
110.0	-0.160±0.055	-0.111±0.070	-0.032±0.120	-0.019±0.036	-0.050±0.041	-0.047±0.068
120.0	-0.122±0.071	-0.395±0.106	-0.602±0.227	-0.165±0.052	-0.120±0.059	-0.253±0.112
130.0	-0.089±0.048	-0.267±0.063	-0.073±0.104	-0.106±0.037	-0.206±0.043	-0.225±0.070
140.0	-0.167±0.080	-0.281±0.106	-0.479±0.222	-0.149±0.069	-0.045±0.074	-0.326±0.128
150.0	-0.175±0.046	-0.220±0.056	-0.568±0.126	-0.098±0.045	-0.187±0.040	-0.210±0.070
160.0	-0.014±0.083	-0.252±0.102	-0.674±0.211	0.064±0.097	-0.071±0.074	-0.243±0.138
170.0	-0.044±0.047	-0.270±0.053	-0.462±0.108	-0.049±0.068	-0.128±0.043	-0.333±0.075

θ_γ (deg)	LAC small HE angles (21.2°)			LAC large HE angles (27.8°)		
	LE angle 14.0°	LE angle 22.0°	LE angle 28.0°	LE angle 14.0°	LE angle 22.0°	LE angle 28.0°
15.0	0.366±0.462	-0.019±0.082	-0.230±0.091		0.110±0.139	-0.054±0.081
30.0	-0.065±0.064	-0.124±0.050	-0.039±0.068	-0.075±0.114	-0.093±0.047	0.010±0.054
40.0	-0.093±0.054	-0.066±0.050	-0.170±0.074	-0.016±0.064	-0.051±0.043	-0.030±0.056
50.0	0.000±0.035	-0.031±0.033	-0.006±0.047	0.030±0.034	0.080±0.027	0.072±0.038
60.0	-0.074±0.056	-0.100±0.056	-0.060±0.079	0.070±0.049	0.112±0.044	0.119±0.061
70.0	0.044±0.037	-0.018±0.038	-0.055±0.057	0.054±0.032	0.054±0.029	0.078±0.044
80.0	-0.016±0.063	-0.067±0.074	0.021±0.101	0.097±0.058	0.050±0.055	0.079±0.088
90.0	0.117±0.041	-0.025±0.046	0.017±0.073	0.004±0.036	0.007±0.035	0.059±0.054
100.0	-0.058±0.067	-0.003±0.075	0.108±0.113	0.091±0.060	-0.075±0.059	-0.151±0.094
110.0	-0.049±0.038	-0.028±0.044	-0.013±0.070	0.009±0.039	0.053±0.036	0.056±0.057
120.0	-0.044±0.038	-0.147±0.043	-0.002±0.070	0.046±0.042	0.048±0.037	0.076±0.056
130.0	-0.003±0.041	-0.149±0.046	-0.185±0.076	0.053±0.053	-0.032±0.039	-0.119±0.063
140.0	-0.046±0.074	-0.238±0.082	-0.300±0.128	0.014±0.109	-0.018±0.074	-0.117±0.110
150.0	0.052±0.053	-0.122±0.051	-0.183±0.080	0.017±0.089	-0.019±0.049	-0.127±0.076
160.0	-0.055±0.108	-0.023±0.094	-0.163±0.141	-0.026±0.208	0.136±0.095	-0.266±0.135
170.0	-0.130±0.152	0.079±0.106	-0.297±0.144	0.126±0.435	0.005±0.114	-0.075±0.141

ber of incident beam protons.

Some errors in measurement arise from uncertainties in determining the solid angles subtended by the detectors. For the Cherenkov counters $\Delta\theta_\gamma/\theta_\gamma$ (where θ_γ is the angular range and $\Delta\theta_\gamma$ its uncertainty) ranged from 0.3% to 0.6%. For the LE detectors $\Delta\Omega_{LE}/\Omega_{LE}$ was estimated to be 3.2%, and for the HE detectors $\Delta\Omega_{HE}/\Omega_{HE}$ was 4.7% (SAC) and 6.0% (LAC).

Efficiency calculations were another source of systematic error. The biggest contributor in this category was the uncertainty in the photon detection efficiencies derived through the Monte Carlo code EGS. These stemmed from the following.

(1) Uncertainty in the determination of the absorber thickness between the target and detector, integrated

over the solid angle of the detector. A survey of the calculated detector efficiencies showed that a difference in absorber thickness of 10% resulted in a change in efficiency (at the photon energies of this experiment) of, very roughly, 3%. (A 10% uncertainty in the integrated absorber thickness is probably a conservative estimate.)

(2) Uncertainty in the discriminator thresholds. The code was run for a number of actual detector-absorber combinations, each with a number of different discriminator thresholds centered around 20 MeV. The change in efficiency was found to have only a slight dependence on photon energy and was, on average, 0.7% per MeV change in threshold. An estimated maximum uncertainty in the discriminator thresholds of 7 MeV means an uncertainty in the detector efficiency of 5%.

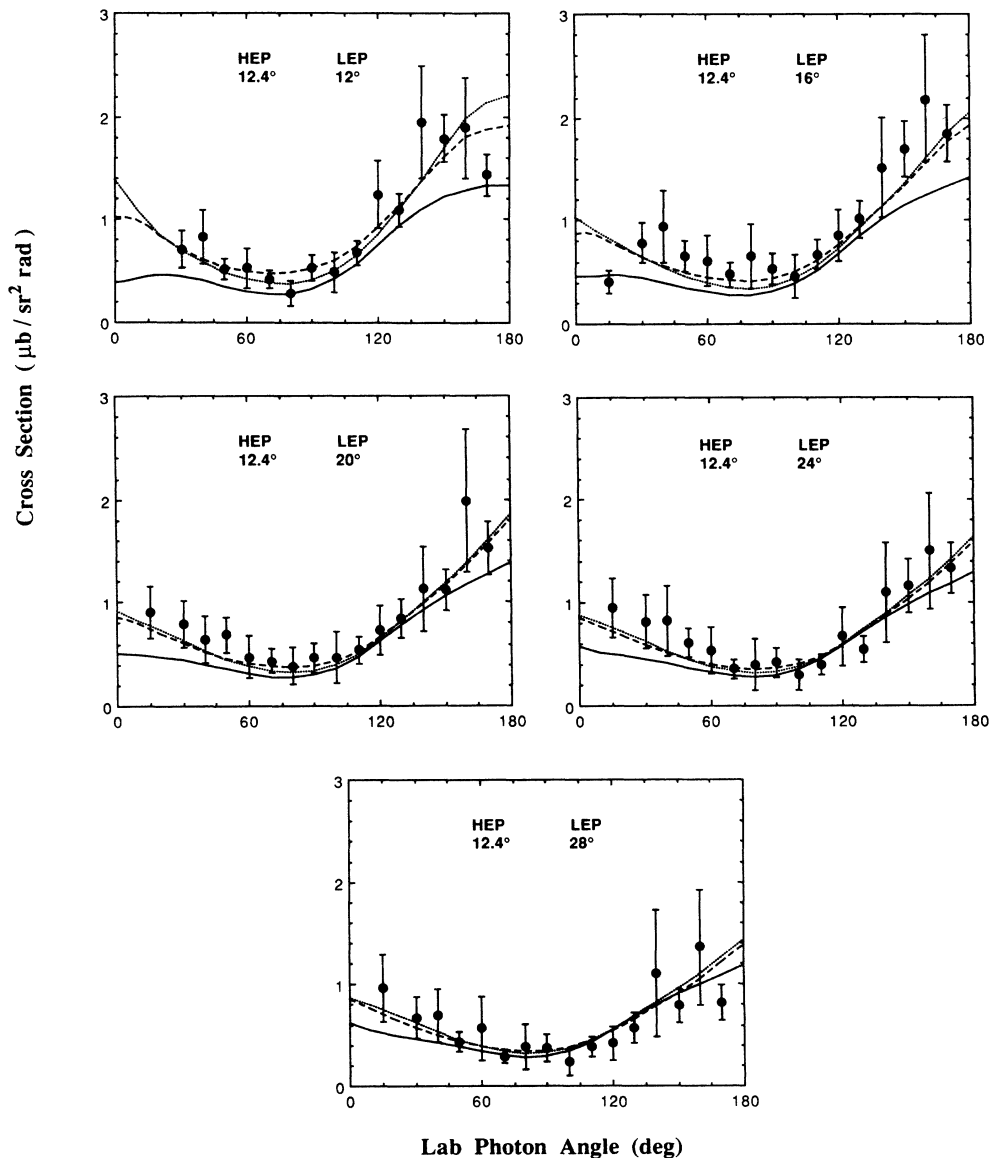


FIG. 8. $pp\gamma$ cross sections for the small-angle SAC. The data are normalized by multiplying by a factor of 0.667. Theoretical curves as in Fig. 6.

(3) Uncertainty inherent in the EGS code itself which must make some simplifications in simulating photon interaction mechanisms. The code's accuracy should be a function of the photon energy and amount of absorbing material, but in the worst case we estimate the error to be less than 10%.

(4) Light collection efficiency. Geometrical effects are hard to estimate but probably not important since tests with 70-MeV electrons gave high efficiencies of around 97%.

Drift-chamber efficiencies were a third source of systematic error. What was important here was the uncertainty in the relative efficiency of the sections of the chambers where pp elastic events and $pp\gamma$ events were detected. The fraction of events with missing coordinates in a given plane varied by less than $\sim 6\%$ between the

two regions (except for the most upstream drift chamber for which it varied by 10%). Furthermore, the relative variation was similar in all planes. The sections of the drift chambers closest to the beam had higher inefficiencies due to unresolved multiple tracks. The absolute inefficiencies due to "multiples" varied by $\sim 10\%$ across a plane. Estimated total uncertainty in the relative wire-chamber efficiency for elastic and $pp\gamma$ events is 2%.

Some other sources of error of significance were the following.

(1) Errors quoted for the fitted values of the elastic cross sections at 16.5° (SAC) and 27.8° (LAC) are both about 1%.¹¹

(2) Error in the correction for the loss of elastic protons due to nuclear reactions in the Cu absorber. This depends on the absorber thickness and the geometry of the

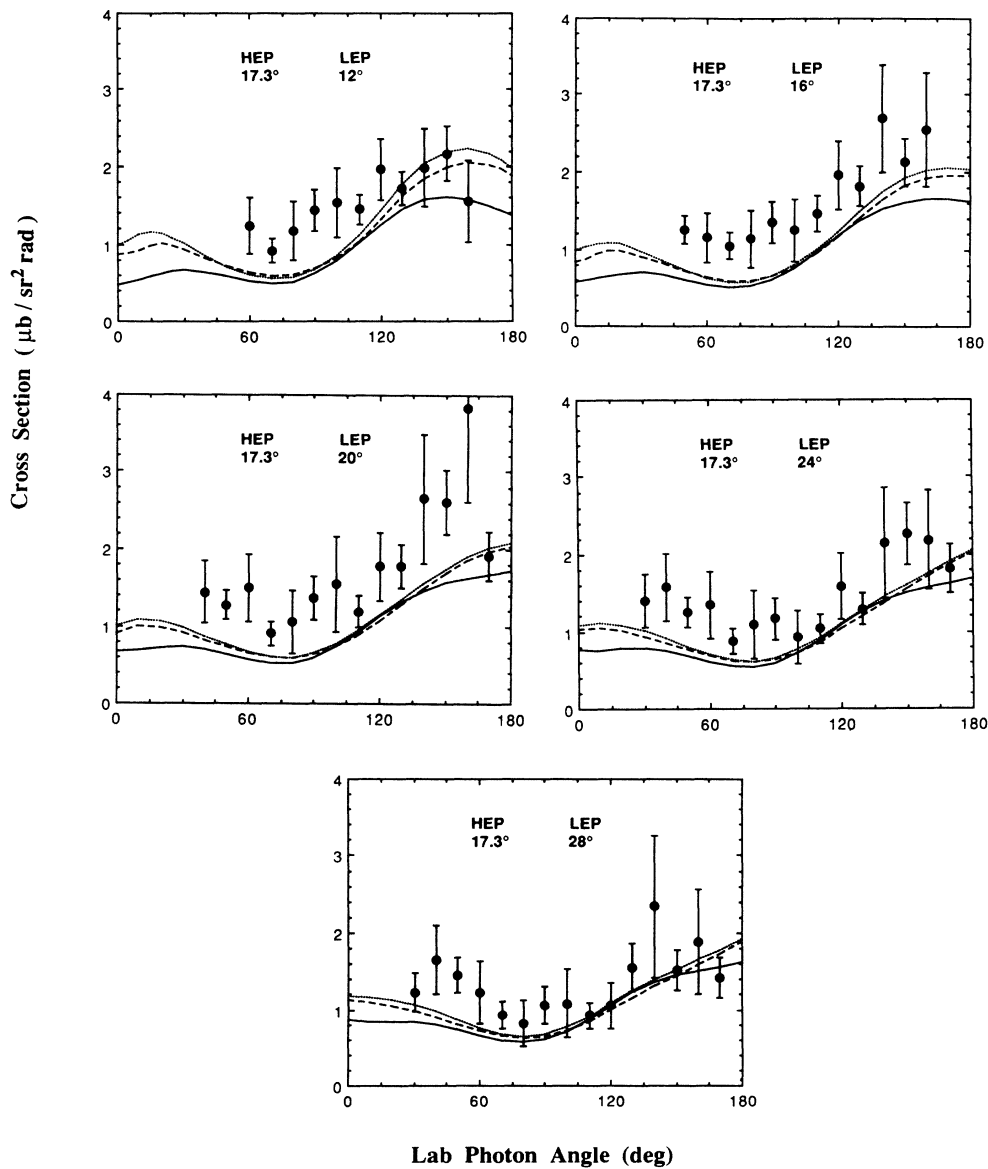


FIG. 9. $pp\gamma$ cross sections for the large-angle SAC. The data are normalized by multiplying by a factor of 0.667. Theoretical curves as in Fig. 6.

scintillator hodoscope. The fraction of protons that undergo a nuclear reaction in the Cu degrader and are not detected was estimated from Ref. 13 to be 18% (LAC) and 22% (SAC). The relative uncertainty in the reaction probability is estimated to be about 10%.¹⁴ This could then affect the cross sections by introducing an uncertainty of 1.8% (LAC) and 2.2% (SAC).

Considering all the above-mentioned sources, the combined total systematic error in the cross section, taking the square root of the sum of the squares of the individual errors, was estimated to be 18% for the worst case of low photon energies at backward photon angles, and slightly smaller at the forward photon scattering angles.

VI. RESULTS AND CONCLUSIONS

A. Outline of potential model calculations

A complete description of the bremsstrahlung calculations of Workman and Fearing which are used for comparison with our data are given in Refs. 9 and 10 for the potential models and in Ref. 15 for the soft-photon approximation. Here we give only a brief summary of the potential model calculations so as to emphasize those ingredients that distinguish these calculations from older ones.

The basic potential model approach is based on the

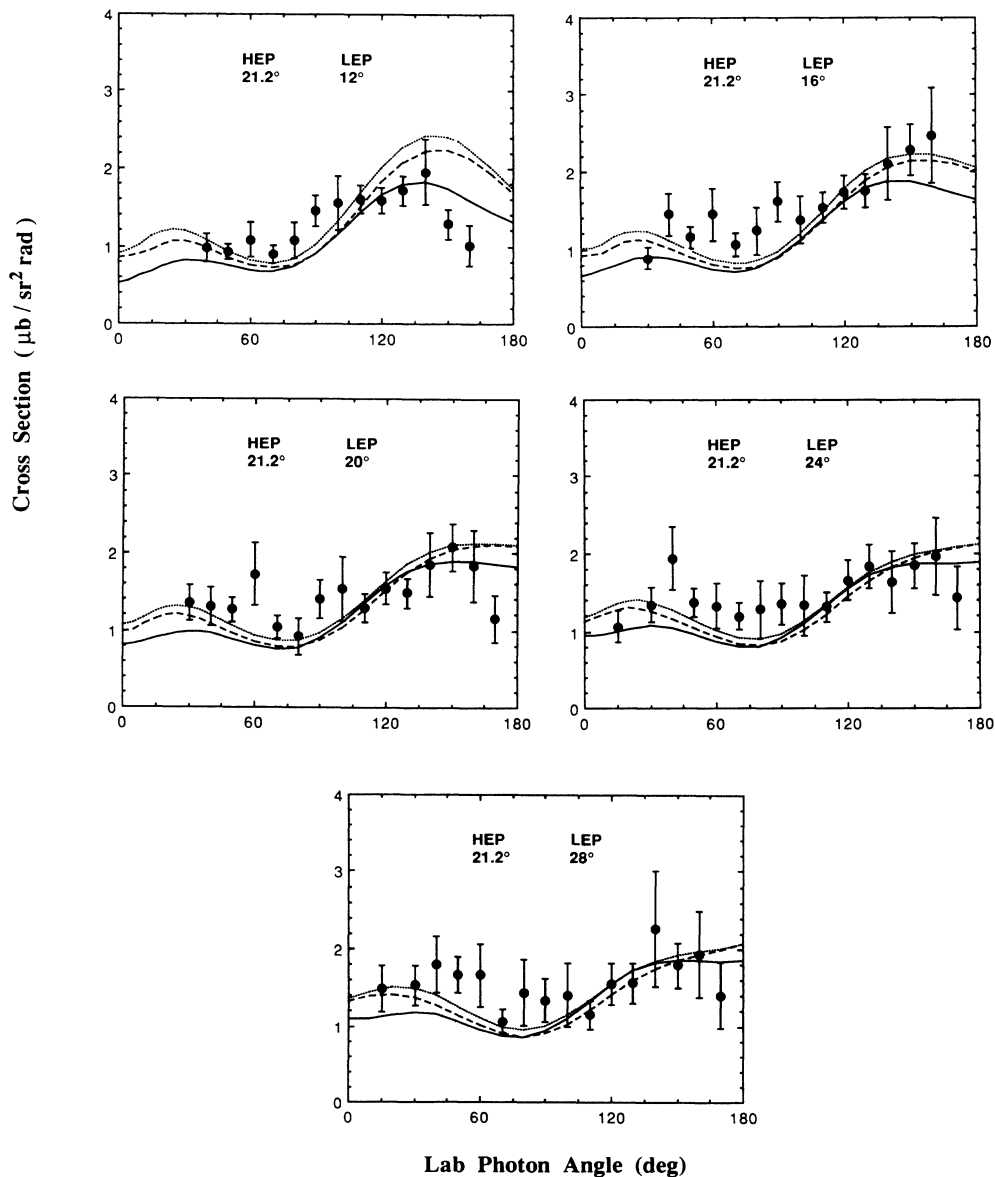


FIG. 10. $pp\gamma$ cross sections for the small-angle LAC. The data are normalized by multiplying a factor of 0.667. Theoretical curves as in Fig. 6.

two-potential formalism of Gell-Mann and Goldberger.¹⁶ In this approach the amplitude for $pp\gamma$ is expressed in terms of matrix elements of the electromagnetic interaction, which is taken to first order only, and in terms of propagators and half-off-shell T -matrix elements. The T -matrix elements incorporate the strong nucleon-nucleon interaction to all orders and, in the present calculation, are obtained for a given potential by solving the Lippmann-Schwinger equation in momentum space.

The most significant new feature of these potential model calculations is the use for the first time of modern theoretically based nucleon-nucleon potentials, notably the Paris and the Bonn potentials. A number of other refinements were also included. In particular some Coulomb corrections were added and one-pion exchange was put in explicitly to account for the higher partial

waves. All phase space and kinematic factors were evaluated relativistically and care was taken with the frame transformations required for the nucleon-nucleon amplitudes. The calculation was done so as to be uniquely gauge invariant through the first two orders in the photon momentum and gauge invariant, though not uniquely so, to all higher orders. The electromagnetic vertex was expanded in powers of $1/m$ and the so-called relativistic spin corrections, which are the important relativistic correction, were kept. Some other smaller relativistic corrections which had not previously been included in such calculations were also kept.

The main contribution not included was the double scattering piece. This comes from situations when the photon emission is both preceded and followed by a strong scattering. Its leading term is proportional to the

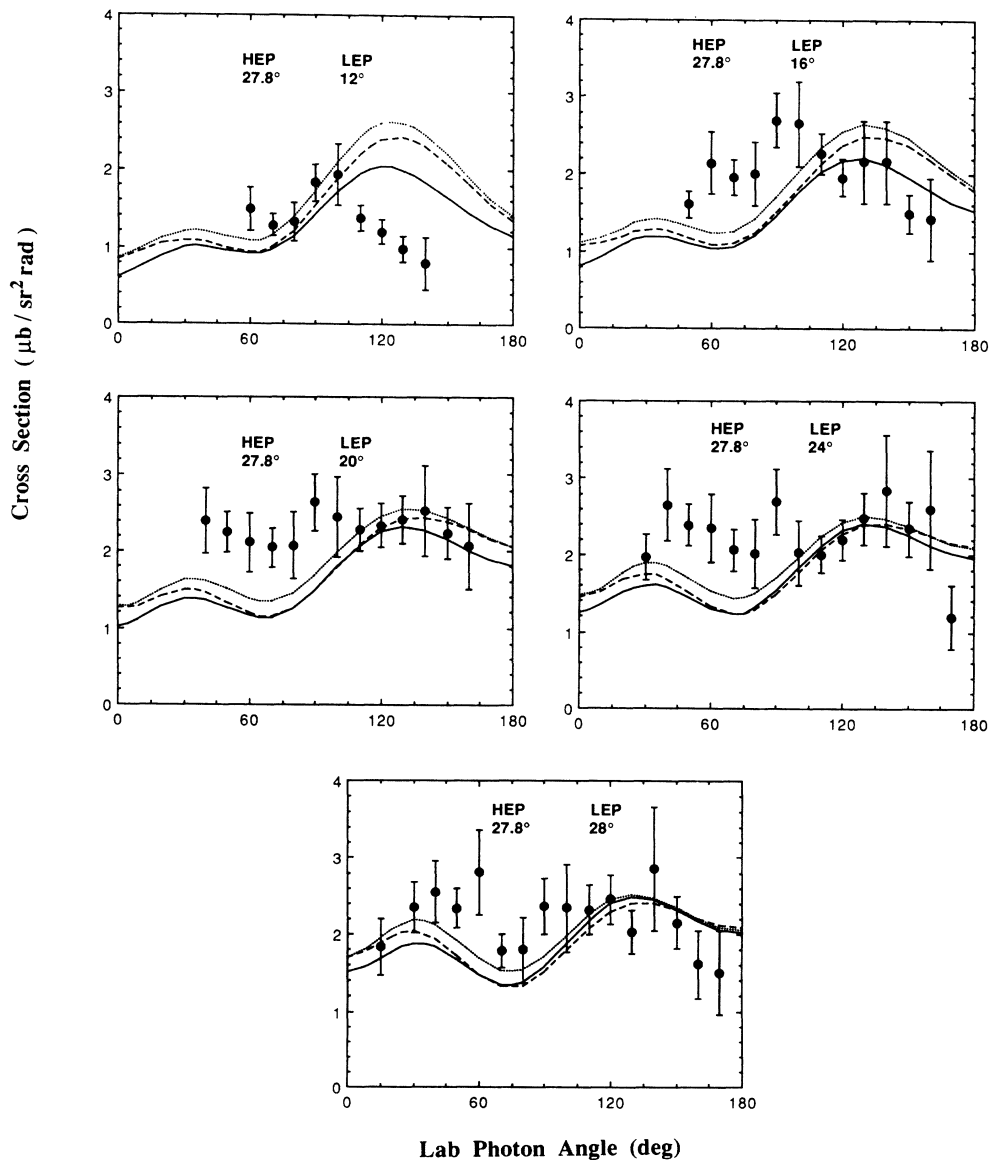


FIG. 11. $pp\gamma$ cross sections for the large-angle LAC. The data are normalized by multiplying by a factor of 0.667. Theoretical curves as in Fig. 6.

TABLE II. $pp\gamma$ cross sections. The values include an arbitrary rescaling factor of 0.667 and correspond to the points plotted in Figs. 8–11. All cross sections are in $\mu\text{b}/\text{sr}^2\text{rad}$.

θ_γ (deg)	SAC small HE angles (12.4°)				
	LE angle 12.0°	LE angle 16.0°	LE angle 20.0°	LE angle 24.0°	LE angle 28.0°
15.0		0.410±0.116	0.899±0.248	0.951±0.287	0.963±0.328
30.0	0.710±0.181	0.733±0.194	0.793±0.223	0.814±0.254	0.675±0.210
40.0	0.834±0.262	0.944±0.344	0.645±0.225	0.822±0.338	0.698±0.261
50.0	0.520±0.098	0.657±0.147	0.689±0.169	0.609±0.139	0.437±0.099
60.0	0.529±0.192	0.613±0.246	0.473±0.206	0.540±0.223	0.566±0.318
70.0	0.423±0.087	0.479±0.115	0.440±0.116	0.356±0.096	0.291±0.071
80.0	0.286±0.119	0.657±0.310	0.389±0.184	0.399±0.246	0.384±0.221
90.0	0.536±0.126	0.530±0.147	0.466±0.145	0.420±0.140	0.371±0.137
100.0	0.491±0.192	0.461±0.208	0.474±0.250	0.296±0.149	0.230±0.135
110.0	0.676±0.112	0.673±0.146	0.544±0.129	0.398±0.099	0.385±0.104
120.0	1.245±0.332	0.858±0.250	0.728±0.234	0.669±0.281	0.418±0.169
130.0	1.089±0.161	1.014±0.182	0.844±0.186	0.552±0.125	0.569±0.152
140.0	1.949±0.545	1.517±0.492	1.126±0.411	1.099±0.486	1.107±0.618
150.0	1.789±0.230	1.698±0.275	1.118±0.195	1.153±0.260	0.788±0.171
160.0	1.891±0.490	2.188±0.613	1.982±0.692	1.504±0.565	1.359±0.565
170.0	1.434±0.204	1.851±0.278	1.523±0.263	1.333±0.248	0.823±0.173

θ_γ (deg)	SAC large HE angles (17.3°)				
	LE angle 12.0°	LE angle 16.0°	LE angle 20.0°	LE angle 24.0°	LE angle 28.0°
15.0					
30.0				1.409±0.346	1.230±0.254
40.0			1.440±0.405	1.579±0.436	1.652±0.445
50.0		1.254±0.186	1.277±0.193	1.258±0.201	1.461±0.232
60.0	1.235±0.366	1.149±0.330	1.496±0.432	1.351±0.442	1.221±0.408
70.0	0.915±0.153	1.044±0.172	0.901±0.160	0.874±0.163	0.925±0.182
80.0	1.173±0.383	1.135±0.370	1.052±0.415	1.091±0.448	0.815±0.305
90.0	1.441±0.267	1.358±0.263	1.365±0.290	1.166±0.275	1.057±0.254
100.0	1.534±0.448	1.256±0.405	1.546±0.624	0.928±0.343	1.081±0.461
110.0	1.450±0.186	1.471±0.226	1.197±0.203	1.035±0.190	0.919±0.169
120.0	1.968±0.392	1.961±0.443	1.777±0.442	1.585±0.434	1.051±0.309
130.0	1.715±0.211	1.823±0.252	1.780±0.284	1.295±0.206	1.561±0.315
140.0	1.988±0.500	2.695±0.691	2.653±0.833	2.147±0.708	2.343±0.915
150.0	2.170±0.357	2.127±0.301	2.611±0.414	2.267±0.393	1.520±0.265
160.0	1.551±0.526	2.549±0.736	3.830±1.211	2.186±0.638	1.883±0.677
170.0			1.916±0.318	1.818±0.313	1.416±0.263

θ_γ (deg)	LAC small HE angles (21.2°)				
	LE angle 12.0°	LE angle 16.0°	LE angle 20.0°	LE angle 24.0°	LE angle 28.0°
15.0				1.060±0.208	1.488±0.296
30.0		0.884±0.142	1.360±0.232	1.341±0.224	1.532±0.254
40.0	0.969±0.182	1.449±0.268	1.306±0.250	1.942±0.406	1.805±0.360
50.0	0.926±0.105	1.150±0.141	1.267±0.154	1.377±0.179	1.667±0.226
60.0	1.082±0.220	1.447±0.333	1.722±0.407	1.324±0.290	1.664±0.407
70.0	0.888±0.115	1.060±0.144	1.046±0.150	1.192±0.175	1.064±0.155
80.0	1.071±0.229	1.232±0.308	0.922±0.237	1.288±0.372	1.432±0.431
90.0	1.451±0.199	1.613±0.262	1.406±0.241	1.355±0.261	1.342±0.277
100.0	1.560±0.346	1.378±0.311	1.531±0.413	1.333±0.383	1.401±0.409
110.0	1.603±0.180	1.540±0.200	1.287±0.176	1.315±0.194	1.149±0.184
120.0	1.587±0.168	1.734±0.211	1.544±0.202	1.660±0.252	1.557±0.266
130.0	1.711±0.193	1.752±0.212	1.483±0.189	1.828±0.281	1.566±0.257
140.0	1.956±0.417	2.103±0.470	1.852±0.417	1.639±0.394	2.262±0.747
150.0	1.287±0.188	2.276±0.328	2.077±0.305	1.844±0.284	1.799±0.289
160.0	1.008±0.270	2.467±0.619	1.832±0.460	1.967±0.502	1.937±0.552
170.0			1.150±0.309	1.433±0.440	1.410±0.432

TABLE II. (*Continued*).

θ_γ (deg)	LAC large HE angles (27.8°)				
	LE angle 12.0°	LE angle 16.0°	LE angle 20.0°	LE angle 24.0°	LE angle 28.0°
15.0					1.831±0.360
30.0				1.966±0.297	2.352±0.331
40.0			2.394±0.426	2.651±0.472	2.549±0.407
50.0		1.596±0.172	2.247±0.265	2.388±0.266	2.335±0.258
60.0	1.490±0.280	2.137±0.402	2.112±0.388	2.349±0.443	2.804±0.560
70.0	1.274±0.141	1.948±0.235	2.043±0.256	2.061±0.268	1.781±0.212
80.0	1.321±0.251	1.996±0.417	2.073±0.436	2.013±0.451	1.801±0.421
90.0	1.830±0.239	2.698±0.358	2.640±0.371	2.687±0.429	2.362±0.367
100.0	1.935±0.395	2.658±0.553	2.446±0.523	2.027±0.419	2.343±0.572
110.0	1.366±0.165	2.258±0.263	2.285±0.284	2.007±0.245	2.322±0.330
120.0	1.197±0.151	2.262±0.266	2.335±0.286	2.203±0.266	2.455±0.330
130.0	0.977±0.159	1.958±0.242	2.418±0.311	2.474±0.337	2.031±0.275
140.0	0.790±0.340	2.161±0.538	2.532±0.590	2.841±0.729	2.857±0.806
150.0		1.487±0.255	2.234±0.340	2.339±0.359	2.157±0.341
160.0		1.418±0.527	2.067±0.567	2.590±0.774	1.616±0.436
170.0				1.185±0.415	1.505±0.550

total momentum in the center of mass so the calculation was done in the center of mass to suppress this contribution. The full calculation of these terms has been done at lower energies by Heller and Rich¹⁷ and by Brown¹⁸ who found they contributed by of the order of 15% or less, depending on the geometry, at 158 MeV. Some additional gauge terms coming from the momentum dependence of the potential were also not included. These momentum-dependent terms are very difficult to calculate consistently with a given potential and as yet have never been computed.¹⁹

B. Comparison—experiment versus theory

The χ^2 of the measured analyzing powers with respect to the Bonn and Paris potential calculations, as well as the soft-photon approximation, are listed in Table III. For the larger-angle pairs, which generally have lower photon energies and correspond more closely to on-shell situations, both potential models and the SPA predict similar small analyzing powers and our analyzing power results are consistent with these predictions. For the smallest proton angles, which correspond to the most off-shell situations, potential model and SPA predictions

are quite different. Our results follow the potential model calculations and disagree strongly with the SPA predictions. We take this as some of the first unequivocal evidence in proton-proton bremsstrahlung for the importance of non-soft-photon contributions.

For many of the proton angle pairs the measured cross sections show a dependence on θ_γ which is similar to that of the potential model calculations, but with a different normalization. For $\theta_{\text{HEP}}=12.4^\circ$ and 21.2° a reasonable agreement is obtained if the data are multiplied by a factor of 0.667. This factor is close to the ratio of inferred to nominal thicknesses of the hydrogen target, although we have found no other reason to reject the elastic-scattering normalization. The cross sections for $\theta_{\text{HEP}}=17.3^\circ$ require a normalization factor of 0.55, while at $\theta_{\text{HEP}}=27.8^\circ$ the measured and calculated angular distributions have different shapes in four out of five cases. If one were to assume the discrepancy to be due to measurement error, rather than shortcomings of the theory, error in overall normalization and errors in calculating photon detection probability are the most likely sources. However, a simple renormalization of the data does not account for all the discrepancies observed. The elastic-scattering data

TABLE III. χ^2 per data point for the analyzing power data in Figs. 6 and 7. Each χ^2 value includes 16 points.

LEP angle (deg)	SPA	Bonn	Paris	SPA	Bonn	Paris
SAC HEP angle=12.4°			SAC HEP angle=17.3°			
14.0	10.84	0.845	1.282	8.078	2.429	2.352
22.0	5.566	0.986	1.743	6.308	2.056	2.078
28.0	1.272	1.545	1.393	2.203	1.272	1.352
LAC HEP angle=21.2°			LAC HEP angle=27.8°			
14.0	4.191	1.814	1.842	1.998	0.782	0.950
22.0	2.272	1.549	1.329	3.264	2.219	2.448
28.0	1.498	1.108	1.052	2.584	1.860	1.983

was analyzed independently a second time when the normalization problem became apparent and consistent results were obtained. The estimated error in the normalization is 17%.

Some contributions neglected in the theoretical calculations do increase the cross section. In particular the double scattering terms as calculated at lower energies by Heller and Rich¹⁷ and Brown¹⁸ can be as much as 15% under some circumstances. However, these terms are corrections of higher orders in the photon momentum, as are the other terms which have not been included. Thus they should be largest for the most off-shell cases corresponding to the smallest angle pairs, should decrease as the angles get larger, and should vanish in the extreme soft-photon limit. The fact that the observed normalization discrepancy does not do this but seems to be nearly independent of angle suggests that these terms neglected in the theoretical calculations are not the primary explanation for the difficulties with the normalization.

C. Conclusions

Although the χ^2 values for the analyzing powers tend to favor the Bonn potential, we do not suggest that this experiment can select the most appropriate existing potential for the nuclear force. The statistical errors are, in most bins, larger than the differences between the Paris and Bonn potentials for both the cross sections and the analyzing powers. The kinematics of this experiment meant we were studying the amplitudes at off-shell momenta between 1.0 and 2.5 fm⁻¹, on-shell momenta less than 1.8 fm⁻¹, and at energies where the *P*-wave amplitude is most important. Calculations show that the Bonn and Paris potentials differ most in their off-shell behavior in the *S* wave, which here however gives a fairly small contribution.¹⁵

The most important results of this experiment are the first analyzing power measurements of the bremsstrahlung process and the first comprehensive measurements of both cross sections and analyzing powers over a wide range of kinematic conditions. The analyzing powers give the first evidence showing that the off-shell behavior of the nucleon-nucleon force cannot be explained by soft-photon terms alone. We also conclude that both the Paris and Bonn potential models provide a reasonable description of the off-shell nature of the *NN* force as probed by the *pp* γ reaction in this experiment.

ACKNOWLEDGMENTS

This work was supported in part by the Natural Sciences and Engineering Research Council of Canada.

APPENDIX: SUMMARY OF MONTE CARLO CORRECTIONS

In calculating the ratio "ideal"/"real" the following approximations were made.

(1) All events were generated within the 5-mm-thick liquid-hydrogen portion of the target. Without this simplification the geometry would be complicated, making the efficiency for photon detection extremely difficult

to calculate. This approximation is justified since the detectors were shielded from observing most of the gas on either side of the target. Also, good intrinsic resolution of the VDC's gave good definition of the liquid portion of the target, to which a software cut was applied.

(2) No multiple scattering through air was calculated while the HE proton was in the field of the C magnet because of the complication this presents to the ray tracing. The proton was, however, multiple scattered through an equivalent thickness of Cu divided into two sections placed just before and after the field.

(3) The magnetic field dropped to zero at the site of the anode plane of the VDC just downstream of the C magnet. The field was actually approximately 4% of the gap field value in this region. To correct for this, the amplitude of the gap field was increased to give the correct angle of bend for protons of all energies.

1. "Ideal" events

As events were already weighted for phase space by generation uniformly in the center-of-mass system before transforming to the laboratory frame, a cross-section weight was determined by interpolating the square of the matrix element (cross section with phase-space factor divided out) on a four-dimensional grid of the variables θ_γ , θ_{HEP} , θ_{LEP} , and ϕ_{LEP} (obtained after a rotation such that $\phi_{\text{HEP}}=0$). This number was normalized to a value between 0 and 1 by dividing it by the maximum |matrix element|² for the particular configuration, LAC or SAC.

An array element "ideal" (LE,HE,CER) was incremented by an amount equal to the cross-section weight if the following tests were passed: (1) The HEP passed within the active limits of chamber 1; (2) the HEP passed the solid angle cuts on VDC coordinates 2*X* and 2*Y* which were applied to the experimental data; (3) the LEP hit one of the LEP detectors; (4) the photon had a polar angle θ_γ within the polar angle range subtended by one of the Cherenkov detectors.

Each configuration had two HE angle bins; the LAC ranges were 18.0°–24.5° and 24.5°–31.0°; the SAC angle ranges were 9.9°–14.8° and 14.8°–19.8°.

2. "Real" events

A cross-section weight was determined as in the "ideal" case. The efficiency of each photon detector was determined at the upper and lower kinematic limits of the photon energy (for a given LE, HE, and CER bin) with a separate Monte Carlo program EGS. This program determined the total energy deposited within the Pb glass by the electrons and positrons of the shower, which develops as a result of the photoelectric effect, Compton scattering, or pair production by the photon. Input to the program were the type and the amount of material between the event production point and the lead glass, the initial angle with respect to the detector axis, the initial photon energy, and the material and thickness of the detector. The detection efficiency was calculated as the number of events with deposited energy above a 20-MeV discriminator threshold, divided by the total number of events. An

inefficiency correction was included to account for photon events that pair produce or Compton scatter in the absorber before the detector (those photons deposit enough energy to trigger the charged particle veto that was in anticoincidence with the Pb glass detectors). A linear interpolation was made between calculated efficiencies at the two kinematic limits to determine the efficiency at the particular photon energy of the event. Values of this efficiency ranged from 38% for the most backward detected photons (which have the lowest energy), to 71% for the most forward detected photons.

The VDC inefficiencies due to missing and multiple events were determined from events not subjected to the cuts of the skimming process. First, the active area of each VDC plane was divided into four equal sections. The “not missing” fraction on a given plane was calculated as the ratio of the number of events which were good in all planes (i.e., not missing and not multiple) to those events that were good in all planes other than the given plane. The position of the “missing” along a given plane was determined from the position of the track in a neighbor plane. The “not missing” efficiencies varied from chamber to chamber and across each chamber, but averaged about 93% per plane. The percentage “not multiple” was determined from the ratio of events with a good coordinate in each plane to the sum of good events plus those that had at least one multiple coordinate. The combined “not multiple” efficiency over the five planes, calculated as a function of track position on the x -anode plane of the second chamber, averaged about 82%. The real events were weighted for the VDC efficiencies by determining what section of a particular chamber the event passed through, and then assigning the efficiency of

that section to the event.

Corrections for events involving multiple Cherenkov or LE detectors were determined for a given detector from the ratio of those events which had a single Cherenkov (or LE) hit over those that had a single hit plus those that were multiple. The results were roughly 97% and 92%, respectively.

Before an event was accepted and counted, a number of conditions were placed on the energies of the two protons. The energy of the LEP at its detector had to be greater than 1 MeV to be accepted by the discriminators and be less than 143 MeV or it would penetrate the absorber behind its detector and trigger its elastic veto counter. Also the energy of the HEP at its plastic detectors had to be greater than the discriminator threshold of 1 MeV.

In summary, an array “real” (LE,HE,CER) was incremented by an amount equal to the product of the weights of the cross section. VDC “not multiple” and “not missing” efficiencies, Cherenkov and detection and “not multiple” efficiencies, and LE “not multiple” efficiency, if the following tests were satisfied: (1) The HEP passed within the active limits of all drift chambers; (2) the HEP passed within solid angle cuts on anode planes $2X$ and $2Y$ that were applied to the experimental data; (3) the HEP passed within the physical limits of the C magnet; (4) the HEP passed within the physical limits of its plastic trigger counters; (5) the energy of the HEP at its trigger counters was above 1 MeV; (6) the LEP hit one of its detectors; (7) the energy of the LEP at its detector was above a 1-MeV threshold; (8) the energy of the LEP at its detector was below 143 MeV; (9) the photon passed within the physical limits of a Cherenkov detector.

-
- ¹M. L. Halbert, in *The Two-Body Force in Nuclei*, edited by S. M. Austin and G. M. Crawley (Plenum, New York, 1972), p. 53.
- ²J. V. Jovanovich, L. G. Greeniaus, J. McKeown, T. W. Miller, D. G. Peterson, W. F. Prickett, K. F. Suen, and J. C. Thompson, *Phys. Rev. Lett.* **26**, 277 (1971).
- ³L. G. Greeniaus, J. V. Jovanovich, R. Kerchner, T. W. Miller, C. A. Smith, and K. F. Suen, *Phys. Rev. Lett.* **35**, 696 (1975).
- ⁴J. V. Jovanovich, C. A. Smith, and L. G. Greeniaus, *Phys. Rev. Lett.* **37**, 631 (1976).
- ⁵B. M. K. Nefkens, O. R. Sander, and D. I. Sober, *Phys. Rev. Lett.* **38**, 876 (1977).
- ⁶B. M. K. Nefkens, O. R. Sander, D. I. Sober, and H. W. Fearing, *Phys. Rev. C* **19**, 877 (1979).
- ⁷B. M. K. Nefkens, O. R. Sander, D. G. L. Webster, and D. I. Sober, *Phys. Rev. C* **22**, 690 (1980).
- ⁸J. G. Rogers, J. L. Beveridge, D. P. Gurd, H. W. Fearing, A. N. Anderson, J. M. Cameron, L. G. Greeniaus, C. A. Goulding, C. A. Smith, A. W. Stetz, J. R. Richardson, and R. Frascaria, *Phys. Rev. C* **22**, 2512 (1980).
- ⁹R. L. Workman, M.Sc. thesis, University of British Columbia,

1984.

- ¹⁰R. L. Workman and Harold W. Fearing, *Phys. Rev. C* **34**, 780 (1986).
- ¹¹Obtained through SAID (Scattering Analysis Interactive Dial-in program) by R. A. Arndt and L. D. Roper, which calculates NN observables from partial-wave solutions based on a compilation of up-to-date experimental databases; R. A. Arndt *et al.*, *Phys. Rev. C* **28**, 97 (1983).
- ¹²The SPA calculations were done specifically for this experiment. Details of the calculations are available from H. W. Fearing.
- ¹³D. F. Measday and C. Richard-Serre, CERN Yellow Report No. 69-17.
- ¹⁴D. F. Measday (private communication).
- ¹⁵Harold W. Fearing, *Phys. Rev. C* **22**, 1388 (1980).
- ¹⁶M. Gell-Mann and M. L. Goldberger, *Phys. Rev.* **91**, 398 (1953).
- ¹⁷L. Heller and M. Rich, *Phys. Rev. C* **10**, 479 (1974).
- ¹⁸V. Brown, *Phys. Lett.* **25B**, 506 (1967); *Phys. Rev.* **177**, 1498 (1969).
- ¹⁹Harold W. Fearing, *Nucl. Phys.* **A463**, 95 (1987).